

# High-Precision Printing Sandwich Flexible Transparent Silver Mesh for Tunable Electromagnetic Interference Shielding Visualization Windows

Qixiang Wang,<sup>§</sup> Yuhui Feng,<sup>§</sup> Feifei Lin, Yuzhe Chen, Ning Ding, Yijie Zhang, Shujuan Liu, Weiwei Zhao,\* and Qiang Zhao\*



Cite This: *ACS Appl. Mater. Interfaces* 2024, 16, 70644–70655



Read Online

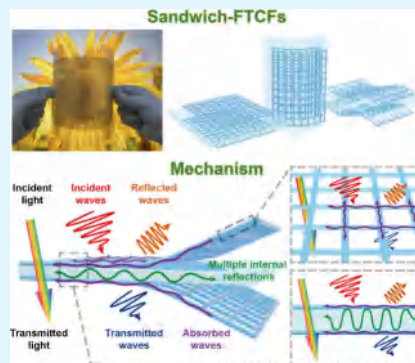
ACCESS |

Metrics & More

Article Recommendations

Supporting Information

**ABSTRACT:** Flexible transparent conductive films (FTCFs) with electromagnetic interference (EMI) shielding performance are increasingly crucial as visualization windows in optoelectronic devices due to their capabilities to block electromagnetic radiation (EMR) generated during operation. Metal mesh-based FTCFs have emerged as a promising representative in which EMI shielding effectiveness (SE) can be enhanced by increasing the line width, reducing the line spacing, or increasing mesh thickness. However, these conventional approaches decrease optical transmittance or increase material consumption, thus compromising the optical performance and economic viability. Hence, a significant challenge still remains in the realm of metal mesh-based FTCFs to enhance EMI SE while maintaining their original optical transmittance and equivalent material usage. Herein, we propose an innovative symmetric structural optimization strategy to create silver mesh-based sandwich-FTCFs with arbitrary customized sizes through high-precision extrusion printing technology for tunable EMI shielding performance. The meticulous adjustment of *xy*-axis offsets and printing starting point ensures perfect alignment of the silver mesh on both sides of the transparent substrate. This approach yields sandwich-FTCFs with optical transmittance equivalent to single-layer-FTCFs under identical parameters while simultaneously achieving up to 40% enhanced EMI SE. This improvement stems from the synergistic effect of multiple internal reflections and wave interference between the symmetric silver meshes. The excellent shielding performance of sandwich-FTCFs is evidenced through effectively blocking electromagnetic waves from common devices such as mobile phones, Bluetooth earphones, and smartwatches. Our work represents a significant advancement in balancing optical transmittance, EMI SE, and material efficiency in high-performance and cost-effective FTCFs.



**KEYWORDS:** flexible transparent conductive films, high-precision printing technology, sandwich silver meshes, symmetric structural optimization strategy, tunable electromagnetic interference shielding performance

## 1. INTRODUCTION

The rapid development of optoelectronic devices is inevitably accompanied by serious electromagnetic radiation (EMR) pollution, which can disturb the normal operation of electronics and even threaten human health.<sup>1–4</sup> This serious problem urgently requires the development of flexible transparent conductive films (FTCFs) that can block electromagnetic interference (EMI) as well as ensure the visual observation for optoelectronic devices.<sup>5–8</sup> Metal mesh-based FTCFs have emerged as promising candidates for EMI shielding. For example, silver mesh-based FTCFs have been widely used for EMI shielding because silver has high electrical conductivity ( $6.2 \times 10^7 \text{ S m}^{-1}$ ), chemical stability, and ductility.<sup>9–11</sup> In general, there are three primary methods to enhance the EMI shielding effectiveness (SE) of metal mesh-based FTCFs by increasing the line width, reducing the line spacing, or increasing mesh thickness.<sup>12,13</sup> However, these approaches often result in reduced optical transmittance or

increased material usage, creating a challenging trade-off between EMI SE, optical performance, and cost effectiveness. Consequently, a significant challenge still remains in enhancing the EMI SE of metal mesh-based FTCFs while maintaining their original optical transmittance and equivalent material usage.<sup>14</sup>

The rational construction of multilayer structures is considered as a representative structural optimization strategy for achieving adjustable EMI SE.<sup>15–18</sup> For instance, our group pioneer the discovery that EMI SE can be improved by stacking individual  $\text{Ti}_3\text{C}_2$  films into a multilayer structure.<sup>19</sup>

Received: September 24, 2024

Revised: November 29, 2024

Accepted: December 2, 2024

Published: December 12, 2024



Furthermore, we demonstrate that the EMI SE can be fine-tuned within a range of 51.1–74.9 dB by adjusting the interlayer spacing. To date, no studies have been reported to develop a multilayer structure that enhances the EMI SE of metal mesh-based FTCFs while maintaining their original optical transmittance and equivalent material usage. The key factor of this challenge lies in achieving perfect symmetry between the metal mesh layers, which is crucial for retaining the optical transmittance. Any deviation from this symmetry will inevitably result in a reduced optical transmittance. Accordingly, a high-precision manufacturing process is highly desirable to meet these requirements. Extrusion printing technology is a high-precision additive manufacturing method that enables the deposition of inks with suitable rheological properties onto substrates of various geometric shapes at room temperature, which offers significant designability and high degree of customization.<sup>20–23</sup> Moreover, this technology offers a cost-effective alternative to traditional processes such as photolithography and screen printing.<sup>24–27</sup> It eliminates the need for expensive equipment and custom masks, thereby, significantly reducing production costs. For example, Tyagi et al. successfully employed extrusion printing technology to repeatedly print silver meshes with varying aspect ratios on a single side of amorphous indium tin oxide (ITO) thin films and achieved an enhancement of the conductivity without compromising optical transmittance.<sup>28</sup> This technology thus demonstrates significant potential for the structural optimization of metal mesh-based FTCFs. However, in-depth research in this specific area remains unexplored.

Herein, we first propose a symmetric structural optimization strategy for precisely printing two fully symmetric silver mesh layers on both sides of a flexible transparent polyethylene terephthalate (PET) substrate through extrusion printing technology to fabricate silver mesh-based sandwich-FTCFs (hereinafter termed sandwich-FTCFs) with arbitrary customized sizes and tunable EMI performance. Specifically, sandwich-FTCFs exhibit superior EMI SE to silver mesh-based single-layer-FTCFs (hereinafter termed single-layer-FTCFs) with identical parameters (i.e., material usage, line width, line spacing, and substrate). The underlying mechanism can be attributed to the synergistic effect of multiple internal reflections and multiple-wave interference between two symmetric silver meshes. Simultaneously, the optical transmittance of sandwich-FTCFs remains constant as single-layer-FTCFs owing to the complete symmetry between the silver mesh layers. Additionally, expanding the interlayer spacing enhances their EMI SE by 40% compared to single-layer-FTCFs, which is primarily ascribed to the enhancement of multiple internal reflections and multiple-wave interference. Furthermore, the sandwich-FTCFs demonstrate exceptional mechanical flexibility, durability, environmental adaptability, photothermal responsiveness, and remarkable EMI shielding capabilities against radiation emanating from common portable electronic devices. The novel symmetric structural optimization strategy paves the way to improve the EMI SE of metal mesh-based FTCFs while preserving their original optical transmittance and equivalent material usage and provides fresh insight into the FTCFs' structure-performance relationships.

## 2. EXPERIMENTAL SECTION

**2.1. Materials.** Flexible transparent PET substrates were purchased from Hengda Automation Technology Co., Ltd. (Taizhou, China). Low-temperature curing conductive silver paste (SP-1027, ≥

70 ± 2%) was purchased from Guangdong Nanhai ETEB Technology Co., Ltd. (Foshan, China). Ethyl acetate was purchased from Changshu Hongsheng Fine Chemical Co., Ltd. (Changshu, China). Hydrochloric acid (HCl, 36–38%) was purchased from Yonghua Chemical Co., Ltd. (Suzhou, China). Sodium hydroxide (NaOH, ≥ 96%) was purchased from Xilong Scientific Co., Ltd. (Shantou, China). 3 M Scotch tape (600-CQ33) was purchased from 3 M Materials Technology Co., Ltd. (Suzhou, China).

**2.2. Fabrication of Sandwich-FTCF.** Initially, silver ink was produced by adding ethyl acetate (400 μL) to silver paste (2 mL) and mixing thoroughly. Subsequently, plasma pretreatment (100 W, 2 min) was used to improve the printability of the PET substrate. Next, extrusion printing technology was used to print a high-resolution silver mesh on the PET substrate. Then the substrate was flipped and another layer of silver mesh was printed via an optical positioning system so that the upper and lower layers of silver mesh completely overlapped to obtain the sandwich conductive film. Finally, the film was conductively treated under vacuum at 100 °C for 30 min to obtain sandwich-FTCF.

**2.3. Characterization.** The silver meshes were cured in a vacuum-drying oven (DZF-6020, Jinghong) at ambient temperature. Scanning electron microscopy (SEM) images of the silver meshes were characterized by a field emission scanning electron microscope (S-4800, Hitachi). EMI SE of sandwich-FTCFs was measured by a rectangular waveguide (WR-90) using a 2-port network analyzer (ENAS071C, Keysight) at the frequency range of 8.2–12.4 GHz. Optical transmittance of sandwich-FTCFs was determined using a UV-vis spectrophotometer (UV-2600, Shimadzu) in the wavelength range of 400–800 nm. The sheet resistance of sandwich-FTCFs was tested by a dual electric digital four-probe tester (ST2263, Suzhou Lattice Electronics Co., Ltd.). ΔR of sandwich-FTCFs was measured by using a digital bridge (E4980A, Keysight) and an electrochemical workstation (CHI660E, CH Instruments). The bending fatigue test of sandwich-FTCFs was completed by the electronic universal material testing machine (3365, Instron). The ultrasonic stability test of sandwich-FTCFs was demonstrated by an ultrasonic cleaner (KH-600 KDB, Hechuang Ultrasonic). The adhesion test of the silver mesh was completed by 3 M Scotch tape. The photothermal effect of sandwich-FTCFs was measured by MW-GX-785/2000 mW, MW-GX-730/1300 mW, and MW-GX-690/500 mW lasers (Changchun Laser Optoelectronics Technology Co., Ltd.), and the laser power meter (VLP-2000, Ranbond) was used to measure their power. The photothermal performance analysis of sandwich-FTCFs was obtained by infrared camera (E40, FLIR). The EMR value of mobile phones, Bluetooth earphones, and smartwatches is measured by the EMR tester (TES-92, TES).

**2.4. EMI Shielding Measurement.** The EMI SE of FTCFs was measured by a WR-90 rectangular waveguide using a 2-port vector network analyzer (E5071C ENA, Keysight Technologies, USA). FTCFs are cut into rectangular sizes of 22.84 × 10.14 mm<sup>2</sup>. The scattering parameters ( $S_{11}$  and  $S_{21}$ ) are collected in X-band frequency range (8.2–12.4 GHz). The coefficients of the reflection ( $R$ ), absorption ( $A$ ), and transmission ( $T$ ) were calculated, followed by the following equations:

$$R = |S_{11}|^2 \quad (1)$$

$$T = |S_{21}|^2 \quad (2)$$

$$A = 1 - R - T \quad (3)$$

The total EMI SE ( $SE_T$ ) of FTCFs is defined as the ratio of transmitted energy to the incident energy of the electromagnetic waves. According to the theory,  $SE_T$  is described as the sum of two shielding mechanisms, including the shielding effectiveness of the reflection ( $SE_R$ ) and the shielding effectiveness of the absorption ( $SE_A$ ), which can be given as eq 4.

$$SE_T = SE_R + SE_A \quad (4)$$

The  $SE_R$  and  $SE_A$  can be measured by calculating  $R$ ,  $A$ , and  $T$  as given in eqs 5 and 6.

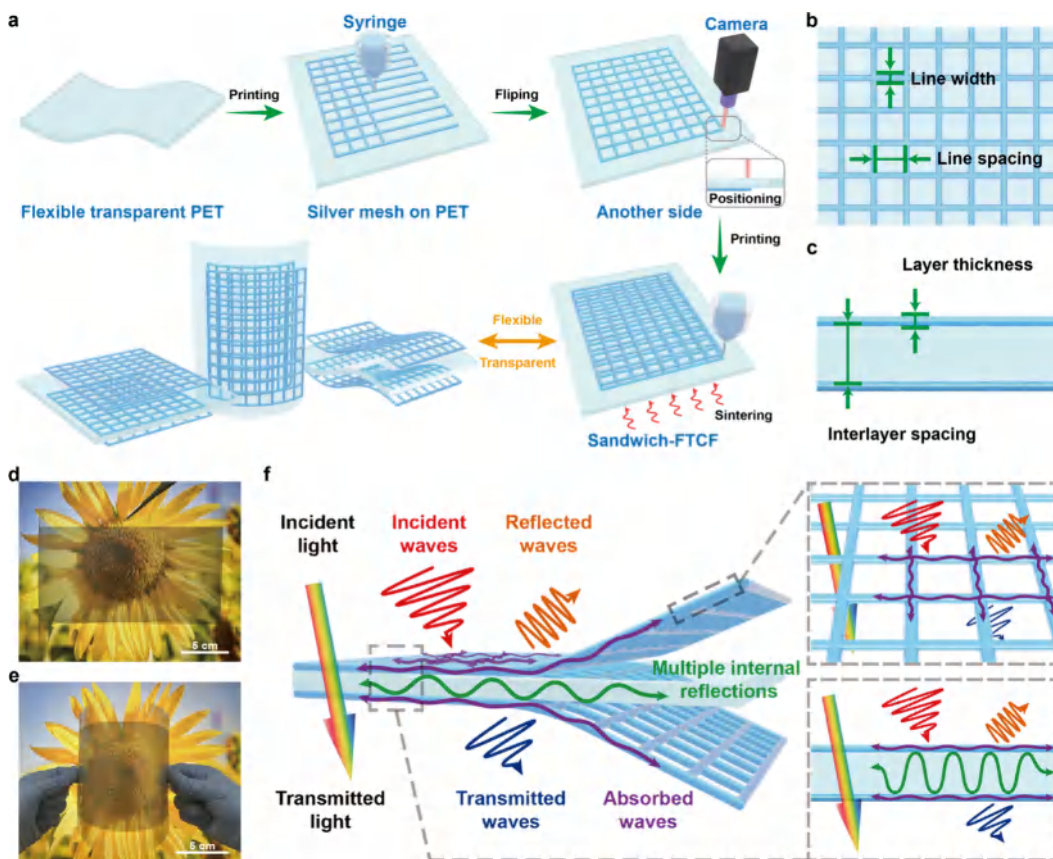


**Figure 1.** (a) Schematic illustration of the fabrication procedure of sandwich-FTCFs. Schematic illustration of (b) top view and (c) side view of sandwich-FTCFs. Photographs of sandwich-FTCFs in (d) flat and (e) bending states (line spacing, 400  $\mu\text{m}$ ; interlayer spacing, 100  $\mu\text{m}$ ). (f) EMI shielding mechanism of sandwich-FTCFs.

$$\text{SE}_R = 10 \log \left| \frac{1}{1 - R} \right| = 10 \log \left| \frac{1}{1 - |S_{11}|^2} \right| \quad (5)$$

$$\text{SE}_A = 10 \log \left| \frac{1 - R}{T} \right| = 10 \log \left| \frac{1 - |S_{11}|^2}{|S_{21}|^2} \right| \quad (6)$$

### 3. RESULTS AND DISCUSSION

**3.1. Design and Fabrication of Sandwich-FTCFs.** Figure 1a schematically illustrates the fabrication process of sandwich-FTCFs with arbitrary customized sizes using extrusion printing technology. The process primarily involves three key steps. (i) The single-layer silver mesh is first printed onto the plasma-treated flexible transparent PET substrate employing extrusion printing technology (Movie S1). (ii) After flipping the PET substrate in place, the  $xy$ -axis offsets are carefully calibrated, and the printing starting point is precisely located. This meticulous adjustment ensures that the symmetric layer of the silver mesh aligns perfectly with the horizontal printing trajectory of the first layer. (iii) Through printing a perfectly symmetric silver mesh on the reverse side of the PET and subsequently sintering the entire structure under vacuum conditions at 100 °C for 30 min, the sandwich-FTCFs are constructed and exhibit good flexibility and optical transmittance. When printing parameters are fixed, both line width and layer thickness are determined (Figure 1b,c). Consequently, the EMI SE and optical transmittance can be tailored on demand solely by adjusting line spacing and interlayer spacing. The sandwich-FTCFs with a line spacing of

400  $\mu\text{m}$  and an interlayer spacing of 100  $\mu\text{m}$  exhibit excellent optical transmittance and flexibility, which also preserves clear visibility of a flower even in a bending state (Figure 1d,e). The underlying mechanism of sandwich-FTCFs for EMI shielding can be systematically proposed as follows (Figure 1f). As the incident electromagnetic waves strike the surface of the top silver mesh that has excellent conductivity and periodic array, the vast majority of incident electromagnetic waves can be reflected due to the significant impedance mismatch between the air and silver mesh.<sup>29–31</sup> The remaining electromagnetic waves undergo multistage attenuation through a sophisticated shielding mechanism. This process involves the absorption of electromagnetic waves due to dielectric loss caused by polarization and ohmic loss resulting from current generated by charge carriers.<sup>32</sup> Additionally, the electromagnetic waves experience multiple internal reflections and multiple-wave interference, which is similar to that observed in Fabry-Pérot resonant cavity structures.<sup>33,34</sup> The line spacing of the silver mesh is between the wavelength of visible light and GHz electromagnetic waves, which means that visible light can pass through the aperture without attenuation but the GHz electromagnetic waves will be partially shielded.<sup>9,35</sup> Meanwhile, sandwich-FTCFs can further enhance multiple internal reflections and multiple-wave interference by adjusting the line spacing and interlayer spacing of the silver mesh, which improves their EMI SE and enables a tunable EMI shielding performance.

**3.2. Influence of Printing Parameters on Silver Mesh.** A high-precision extrusion printing system, which includes a

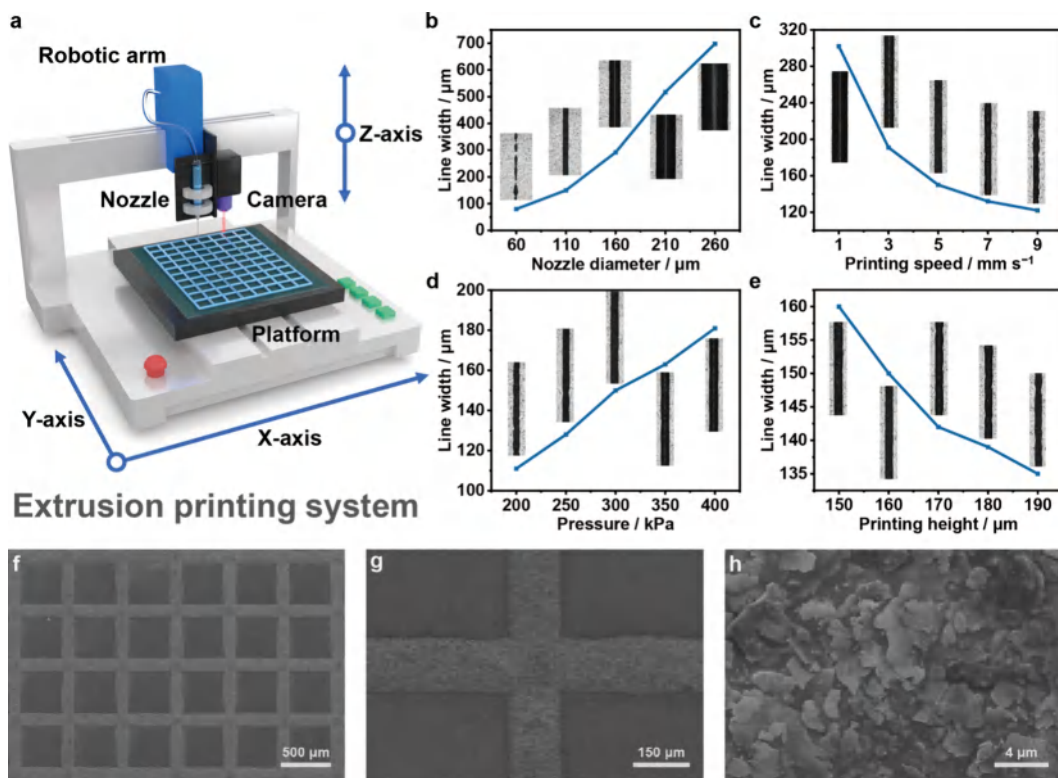


**Figure 2.** (a) Schematic illustration of a high-precision extrusion printing system. Influence of (b) nozzle diameter, (c) printing speed, (d) pressure, and (e) printing height on the line width and surface topography of the silver mesh. Inset: the corresponding optical microscope image. (f–h) SEM images of the silver mesh.

three-axis mechanical system and an optical positioning system, is adopted for directly printing silver meshes (Figure 2a). First, the optical positioning system based on a high-definition camera accurately determines the printing location. Then, the three-axis mechanical system, which consists of a robotic arm ( $x$  axis and  $z$  axis) and a printing platform ( $y$  axis), moves the extrusion nozzle to the designated position. This process guarantees the precise deposition of customized patterns onto the target substrate according to a predefined program. The extrusion printing technology can also be applied to print customized and complex patterns (Figure S1). In order to achieve better structural optimization, high printing resolution is necessary. As the horizontal feature size, the line width of the silver mesh has a significant effect on the printing resolution.<sup>36,37</sup> Specifically, a smaller line width corresponds to a higher resolution.<sup>38</sup> The line width is determined by printing parameters, including nozzle diameter ( $d_n$ ), printing speed ( $v$ ), pressure ( $p$ ), and printing height ( $h$ ).

The influence of the nozzle diameter on the line width and surface topography is initially investigated under certain parameters of  $v = 5 \text{ mm s}^{-1}$ ,  $p = 300 \text{ kPa}$ , and  $h = 160 \mu\text{m}$ . Figure 2b illustrates the relationship between the line width and surface topography of the silver mesh versus the nozzle diameter. The line width is measured as 80, 150, 292, 517, and 698  $\mu\text{m}$  for the nozzle with a diameter of 60, 110, 160, 210, and 260  $\mu\text{m}$ , respectively. Consequently, the smaller nozzle diameter ensures a higher printing resolution, which is consistent with the previously literature.<sup>39</sup> While, for a nozzle diameter of 60  $\mu\text{m}$ , the excessively small diameter hinders the flow of silver inks, resulting in nozzle clogging and eventual breakage of silver lines.<sup>40</sup> When the nozzle diameter is 110, 160, 210, or 260  $\mu\text{m}$ , the silver lines can be printed evenly.

Hence, a nozzle diameter of 110  $\mu\text{m}$  is chosen to achieve high printing resolution.

The influence of printing speed on the line width and surface topography of the silver mesh is subsequently investigated under certain parameters:  $d_n = 110 \mu\text{m}$ ,  $p = 300 \text{ kPa}$ , and  $h = 160 \mu\text{m}$  (Figure 2c). The line width is measured as 302, 191, 150, 132, and 122  $\mu\text{m}$  for the printing speeds of 1, 3, 5, 7, and 9  $\text{mm s}^{-1}$ , separately. When the printing speed increases from 1 to 9  $\text{mm s}^{-1}$ , the line width reduces from 302 to 122  $\mu\text{m}$ , resulting in improved printing resolution due to reduced silver ink deposition per unit time.<sup>41</sup> Printing efficiency determines the overall printing time of the device, that is, a faster printing speed results in a higher printing efficiency.<sup>42</sup> Therefore, as the printing speed increases from 1 to 5  $\text{mm s}^{-1}$ , printing efficiency and printing resolution improve, while the high edge flatness of the silver line well remains. However, when the printing speed increases from 5 to 9  $\text{mm s}^{-1}$ , the edge flatness of the silver line deteriorates due to insufficient silver ink deposition. Accordingly, a printing speed of 5  $\text{mm s}^{-1}$  is selected to balance printing efficiency, printing resolution, and the edge flatness of the silver lines.

The effect of pressure on the line width and surface topography of the silver mesh is further explored under certain parameters of  $d_n = 110 \mu\text{m}$ ,  $v = 5 \text{ mm s}^{-1}$ , and  $h = 160 \mu\text{m}$ . As illustrated in Figure 2d, the line width is measured as 111, 128, 150, 163, and 181  $\mu\text{m}$  under pressures of 200, 250, 300, 350, and 400 kPa, respectively. As the pressure increases from 200 to 400 kPa, the line width expands from 111 to 181  $\mu\text{m}$ , resulting in reduced printing resolution. It is attributed to that the higher pressure causes increased extrusion volume of silver ink per unit time.<sup>43</sup> At pressures of 200 and 250 kPa, the printed lines exhibit unevenness due to the insufficient

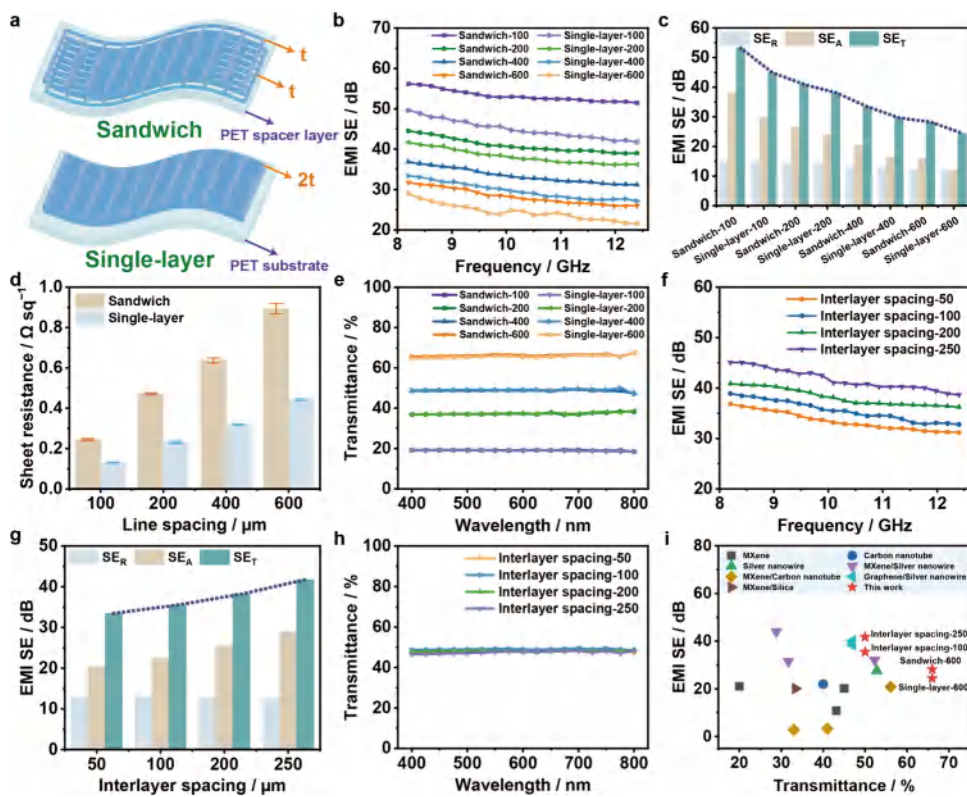


**Figure 3.** (a) Schematic illustration of sandwich-FTCFs and single-layer-FTCFs. (b) EMI SE; (c) SE<sub>T</sub>, SE<sub>A</sub>, and SE<sub>R</sub> values; (d) sheet resistance; and (e) optical transmittance of sandwich-FTCFs and single-layer-FTCFs with different line spacings. (f) EMI SE; (g) SE<sub>T</sub>, SE<sub>A</sub>, and SE<sub>R</sub> values; and (h) optical transmittance of sandwich-FTCFs with different interlayer spacings. (i) Comparison of EMI SE and optical transmittance of sandwich-FTCFs and single-layer-FTCFs with other EMI shielding materials.

extrusion volume of silver inks. However, the lines can be uniformly printed as the pressure increases from 300 to 400 kPa. Thus, 300 kPa is the optimal choice to achieve a balance between printing resolution and uniformity of printed lines.

Finally, the printing height, defined as the distance between the nozzle and the substrate, is investigated under certain parameters of  $d_n = 110 \mu\text{m}$ ,  $v = 5 \text{ mm s}^{-1}$ , and  $p = 300 \text{ kPa}$ . The relationship between the line width and surface topography of the silver mesh versus printing height is shown in Figure 2e. The line width is measured as 160, 150, 142, 139, and 135  $\mu\text{m}$  for the printing heights of 150, 160, 170, 180, and 190  $\mu\text{m}$ , respectively. A higher printing height correlates with a greater printing resolution, which is consistent with previous literature.<sup>44</sup> When the printing height increases from 150 to 160  $\mu\text{m}$ , printing resolution improves, while the edges of the silver lines remain smooth. Nevertheless, as the printing height is beyond 160  $\mu\text{m}$  and up to 190  $\mu\text{m}$ , the edge flatness of the silver line deteriorates. Consequently, a printing height of 160  $\mu\text{m}$  is chosen for the subsequent experiments.

The silver mesh is printed on plasma-treated PET using the optimal printing parameters of  $d_n = 110 \mu\text{m}$ ,  $v = 5 \text{ mm s}^{-1}$ ,  $p = 300 \text{ kPa}$ , and  $h = 160 \mu\text{m}$ . The resulting surface topography is illustrated in Figure 2f–h. SEM images demonstrate that the silver mesh exhibits a homogeneous line width of 150  $\mu\text{m}$  and a line spacing of 400  $\mu\text{m}$ , which align with the theoretical dimensions of the CAD drawing (Figure S2). The minimum lateral size of silver nanosheets is mostly around 2  $\mu\text{m}$ , which is smaller than 1/50 of the nozzle diameter. This provides good printability and validates the rationality of printing parameters.<sup>45</sup> Furthermore, the larger silver nanosheets are formed through the melting and fusion of multiple nanosheet edges

during the sintering treatment.<sup>46</sup> The layer-by-layer accumulation of silver nanosheets enhances contact area and reduces contact resistance which facilitates the efficient charge transfer throughout the network and ensures high conductivity.<sup>47</sup> The viscosity of the silver inks decreases rapidly with the increase in the shear rate (Figure S3a). It proves that silver inks have desirable shear thinning properties, which allows for continuous extrusion and quick solidification. Moreover, the loss modulus ( $G''$ ) of the silver inks is always greater than the storage modulus ( $G'$ ), thus exhibiting liquid-like behaviors (Figure S3b). As the shear stress increases, the difference between the  $G''$  and  $G'$  also increases. It indicates that the silver inks are approaching the liquid state. We successfully printed the silver mesh with a line width of 150  $\mu\text{m}$  and a line spacing of 400  $\mu\text{m}$  on glass, F4B, FR4 and photo paper using silver ink (Figure S4). It proves that our silver ink is universally applicable to the substrate. In addition, we printed five silver lines with line widths of 100, 150, 200, 250, and 300  $\mu\text{m}$  on the PET substrate. These lines are spaced 100  $\mu\text{m}$  apart. The integrated width error is less than 2  $\mu\text{m}$ , which reflects the high precision of the extrusion printing technology (Figure S5).

### 3.3. EMI Shielding Performance of Sandwich-FTCFs.

The silver mesh is printed on the PET substrate using the aforementioned printing parameters to construct sandwich-FTCFs for evaluating the EMI shielding performance. Two configurations of silver mesh-based FTCFs are developed to study the effect of structure on shielding performance (Figure 3a). One configuration is sandwich-FTCFs, where the PET substrate hosts two symmetrically placed silver mesh layers, each with a thickness of  $t$ . The perfect symmetry of the silver mesh in sandwich-FTCFs is demonstrated by the cross-

sectional SEM image (Figure S6). The other configuration is the single-layer-FTCFs, which involves two silver mesh layers tightly stacked on one side of the PET substrate, resulting in a total silver layer thickness of  $2t$ . To explore the impact of line spacings on shielding performance, silver mesh-based FTCFs with varying line spacings of 100, 200, 400, and 600  $\mu\text{m}$  are prepared (Figure S7). The thickness of the PET substrate is 50  $\mu\text{m}$  in all samples.

As depicted in Figure 3b,c, the EMI SE values of sandwich-FTCFs in the X-band (8.2–12.4 GHz) demonstrates a significant inverse correlation with the line spacing of the silver mesh. Specifically, the EMI SE values are 53.2, 40.9, 33.4, and 28.2 dB for line spacings of 100, 200, 400, and 600  $\mu\text{m}$ , respectively. Notably, all FTCFs surpass the basic requirement for commercial applications ( $\sim 20$  dB), which also effectively blocking 99% of incident radiation.<sup>48</sup> The  $\text{SE}_T$  is the sum of  $\text{SE}_R$  and  $\text{SE}_A$ . For sandwich-FTCFs, the corresponding  $\text{SE}_A$  values are 38.2, 26.6, 20.3, and 15.9 dB, while the  $\text{SE}_R$  values are 15.0, 14.3, 13.1, and 12.3 dB for the same sequence of line spacing. In comparison, single-layer-FTCFs demonstrate lower EMI SE values of 44.9, 38.1, 29.6, and 24.4 dB for the respective line spacings, with corresponding  $\text{SE}_A$  values of 29.8, 23.7, 16.4, and 12.1 dB, and  $\text{SE}_R$  values of 15.1, 14.4, 13.2, and 12.3 dB. Throughout all measured parameters, sandwich-FTCFs consistently outperform their single-layer counterparts, showing improvements in EMI shielding performance of up to 18%. This emphasizes the enhanced shielding capabilities of the sandwich configuration.

To elucidate the EMI shielding mechanism, the sheet resistances of both sandwich-FTCFs and single-layer-FTCFs are measured (Figure 3d). The sheet resistance of the sandwich-FTCFs is 0.89, 0.63, 0.47, and 0.24  $\Omega \text{ sq}^{-1}$  for the silver mesh line spacings of 600, 400, 200, and 100  $\mu\text{m}$ , respectively. In comparison, single-layer-FTCFs demonstrate lower sheet resistance values of 0.44, 0.31, 0.23, and 0.13  $\Omega \text{ sq}^{-1}$  for the same line spacings. Notably, the sandwich-FTCFs consistently display higher sheet resistance compared to their single-layer counterparts. This difference can be attributed to two factors: the isolation effect of the PET substrate in the sandwich structure, and the silver content on each side of the PET substrate in sandwich-FTCFs being approximately half that of single-layer-FTCFs. As the line spacing of silver mesh decreases, the sheet resistance of FTCFs is also reduced, while both sandwich-FTCFs and single-layer-FTCFs exhibit improved EMI SE. Their corresponding  $\text{SE}_R$  is all around 15 dB, which is greater than 3 dB. It means that 96.8% of the incident electromagnetic wave is reflected on the surface of the FTCFs (Figure 3c).<sup>49,50</sup> This is attributed to the large impedance mismatch between the air and the silver mesh.<sup>15</sup> Notably, their corresponding  $\text{SE}_A$  values show an upward trend. Absorption is the secondary mechanism for EMI shielding, which can be enhanced by the dielectric loss and ohmic loss.<sup>51</sup> The reduced sheet resistance provides more electron transmission paths and promotes the interaction between charge carriers and incident electromagnetic waves.<sup>14,52</sup> The former leads to greater dielectric loss.<sup>53</sup> Meanwhile, the latter generates a microcurrent to enhance ohmic loss.<sup>32</sup> Accordingly, the surface absorption of electromagnetic waves increases with the decreased line spacing of the silver mesh. Although both sandwich-FTCFs and single-layer-FTCFs have same materials usage, the sandwich-FTCFs have a higher  $\text{SE}_A$  than the single-layer-FTCFs with the same line spacings of silver mesh. This is due to a finite-thick PET substrate is located between two lossy

metal layers for the sandwich configurations, which is similar to a Fabry-Pérot resonant cavity.<sup>33</sup> The silver meshes on both sides of the PET enhance multiple internal reflections and multiple-wave interference, and thus enhancing the absorption attenuation.<sup>54</sup>

In addition to their excellent EMI shielding performance, the optical properties of FTCFs are investigated. Figure 3e illustrates the detailed optical transmittances of both sandwich-FTCFs and single-layer-FTCFs. It shows an upward trend as the line spacings in silver meshes increase. Notably, the optical transmittance of two configurations with the equivalent line spacing in silver mesh-based FTCFs remains nearly identical at the wavelength of 400–800 nm. This consistency is attributed to the fully symmetrical silver mesh on both sides of the PET substrate in sandwich-FTCFs, which allows the same transmitted luminous flux as that in single-layer silver mesh. Sandwich-FTCFs with a line width of 100  $\mu\text{m}$  and a line spacing of 600  $\mu\text{m}$  are fabricated by optimizing the printing parameters to  $d_n = 60 \mu\text{m}$ ,  $v = 6.5 \text{ mm s}^{-1}$ ,  $p = 490 \text{ kPa}$ , and  $h = 50 \mu\text{m}$  (Figure S8a). In comparison with sandwich-FTCFs featuring a line width of 150  $\mu\text{m}$  and the same line spacing of 600  $\mu\text{m}$ , the transmittance is enhanced from 66% to 76% (Figure S8b,c). It demonstrates that the optical transmittance of sandwich-FTCFs can be further improved by adjusting the printing parameters. Furthermore, asymmetric sandwich-FTCFs with various line spacings are fabricated by using a 50  $\mu\text{m}$  thick PET substrate. Although these structures exhibit improved EMI SE compared to single-layer-FTCFs with identical parameters, their optical transmittance is significantly reduced. This finding further confirms the superiority of symmetric sandwich-FTCFs (Figures S9–S11).

Comprehensive consideration of the EMI shielding performance and the optical transmittance, the sandwich-FTCFs with a line spacing of 400  $\mu\text{m}$  are selected for further study. By adjusting the thickness of the PET substrate, sandwich-FTCFs are fabricated with interlayer spacings of 50, 100, 200, and 250  $\mu\text{m}$ . The corresponding EMI SE is measured as 33.4, 35.5, 38.2, and 41.7 dB, respectively (Figure 3f,g). Notably, the sandwich-FTCFs with an interlayer spacing of 250  $\mu\text{m}$  achieve the highest EMI SE. That is because the reflection from the inner surface of the bottom silver mesh will form a standing wave with the antinodal plane (maximum lateral electric field) on the top silver mesh, thereby enhancing absorption caused by multiple internal reflections and multiple-wave interference. The standing wave effect enhances with interlayer spacing and reaches a maximum at a quarter wavelength.<sup>19</sup> As the interlayer spacings increase from 50 to 250  $\mu\text{m}$ ,  $\text{SE}_R$  does not show any significant variation. But  $\text{SE}_A$  significantly increases from 20.3 to 22.4, 25.3, and 29.0 dB, respectively. The optical transmittance of sandwich-FTCFs is 50% (Figure 3h). In contrast, the EMI SE of single-layer-FTCFs with 400  $\mu\text{m}$  line spacing is 29.6 dB when the PET substrate thicknesses are 50, 100, 200, and 250  $\mu\text{m}$ , respectively. Their optical transmittance is also 50%. It demonstrates that PET thickness does not affect EMI shielding performance (Figures S12 and S13). Notably, sandwich-FTCFs achieve up to 40% improvement in EMI SE compared to single-layer-FTCFs with identical parameters. Compared to other FTCFs based on MXene,<sup>14,55,56</sup> carbon nanotube,<sup>57</sup> silver nanowire,<sup>58</sup> and composite materials,<sup>59–65</sup> our sandwich-FTCFs exhibit a satisfactory comprehensive performance (Figure 3i and Table S1).

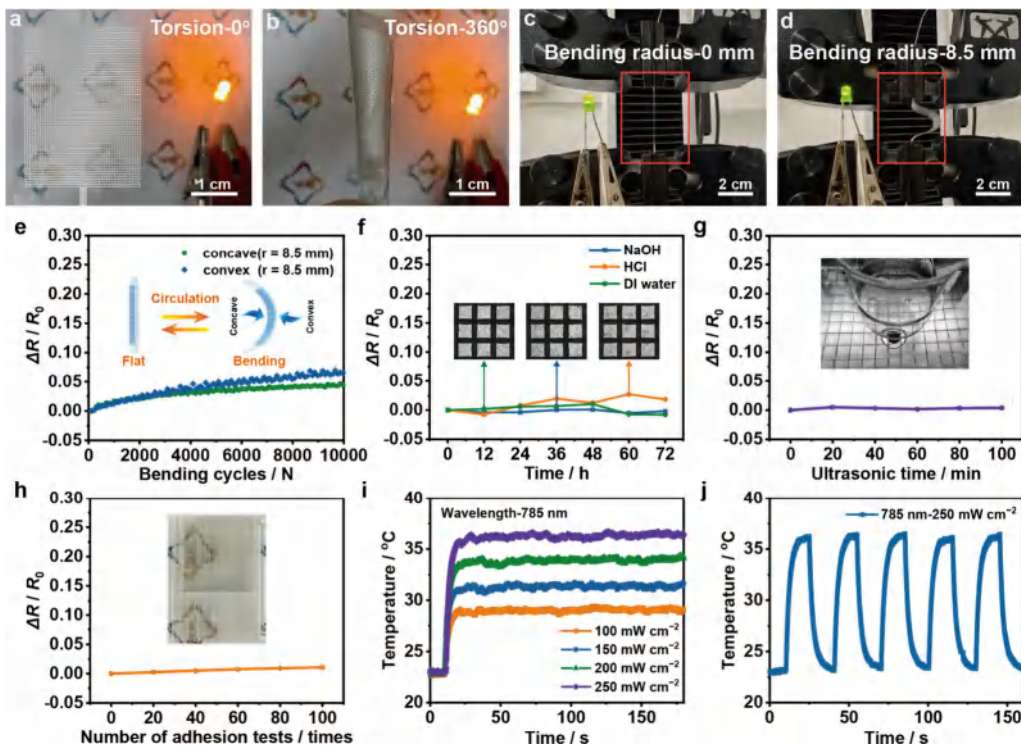


**Figure 4.** Changes of the brightness for lighting an LED lamp in torsion at angles ranging from (a) 0° to (b) 360° and in a bending state with a radius ranging from (c) 0 mm to (d) 8.5 mm.  $\Delta R/R_0$  changes for sandwich-FTCFs after (e) bending cycles, (f) chemical attack (inset: the corresponding optical microscope image), (g) ultrasonic vibration, and (h) adhesion tests. (i) Temperature–time curves of sandwich-FTCFs with varying laser power densities at a wavelength of 785 nm. (j) Temperature–time curves of sandwich-FTCFs under cycles of on–off light illumination at a laser power density of 250  $\text{mW cm}^{-2}$ .

**3.4. Properties of Sandwich-FTCFs.** To meet the EMI shielding requirements of flexible electronic devices, the mechanical flexibility and durability of the sandwich-FTCFs are crucial. The flexibility is initially assessed through torsion and bending tests. The brightness of the LED lamp remains nearly constant during the torsion process of sandwich-FTCFs from 0° to 360° and bending with radius ranging from 0 to 8.5 mm, demonstrating the excellent mechanical flexibility (Figure 4a–d, Figure S14 and Movie S2). To further investigate the durability, the bending fatigue tests with a radius of 8.5 mm over 10,000 cycles are performed (Figure 4e and Movie S3).<sup>66</sup> The relative resistance change ( $\Delta R/R_0$ ) is less than 7% on the convex surface and less than 5% on the concave surface, demonstrating exceptional bending durability. It can be attributed to sandwich-FTCFs having a thin substrate and narrow silver line width, which result in a low curvature radius fracture threshold and superior flexibility. Moreover, the silver mesh on the convex surface experiences tensile loading during bending, while the concave surface undergoes compressive loading. This difference in stress distribution explains the smaller  $\Delta R/R_0$  observed on the concave side.<sup>67</sup>

To cope with different working environments, environmental adaptability is also important for sandwich-FTCFs. Therefore, chemical environmental stability tests are carried out to verify the environmental adaptability of sandwich-FTCFs. Various chemical environments are simulated by immersing sandwich-FTCFs in three kinds of solutions including neutral deionized (DI) water, NaOH (pH = 11), and HCl (pH = 3; Figure 4f).<sup>68</sup> After immersion for 72 h,  $\Delta R/R_0$  of sandwich-FTCFs in DI water and NaOH aqueous solution is less than 1%, while in HCl aqueous solution, it is

less than 2.7%. Additionally, the surface topography of the silver mesh remains unchanged (Figures S15–S18), demonstrating the excellent adaptability of sandwich-FTCFs to different chemical environments. The significant  $\Delta R/R_0$  of sandwich-FTCFs in HCl solution can be attributed to the high chemical reactivity between silver nanosheets and HCl, in which the formed silver chloride (AgCl) leads to the increased electrical resistance.<sup>69</sup> To further test the environmental adaptability, the sandwich-FTCFs undergo an ultrasonic water bath (40 kHz, 600 W). After testing for 100 min,  $\Delta R/R_0$  is less than 0.5%, confirming good adaptability in an ultrasonic concussion environment (Figure 4g). Furthermore, the printed silver mesh requires tight adhesion to the PET substrate to prevent performance degradation resulting from its detachment during the use of sandwich-FTCFs. The 100 peeling tests conducted on the same area of the sandwich-FTCFs are executed to verify the adhesion of the silver mesh (Figure 4h). At the end of the test,  $\Delta R/R_0$  is less than 1%, which indicates strong adhesion and stability of the silver mesh to the PET substrate. This phenomenon arises from plasma treatment, which enhances the hydrophilicity of the substrate and improves the adhesion between the silver mesh and the substrate.<sup>70,71</sup>

Figure 4i illustrates the temperature curve of sandwich-FTCFs under varying laser power densities at a wavelength of 785 nm. Notably, the sandwich-FTCFs rapidly warm from the initial temperature to the saturation temperature in approximately 15 s, which demonstrates the fast-response photothermal conversion ability. The saturation temperature reaches 29 °C at a laser power density of 100  $\text{mW cm}^{-2}$ , and increases to 31, 34, and 36 °C at higher laser power density of 150, 200,

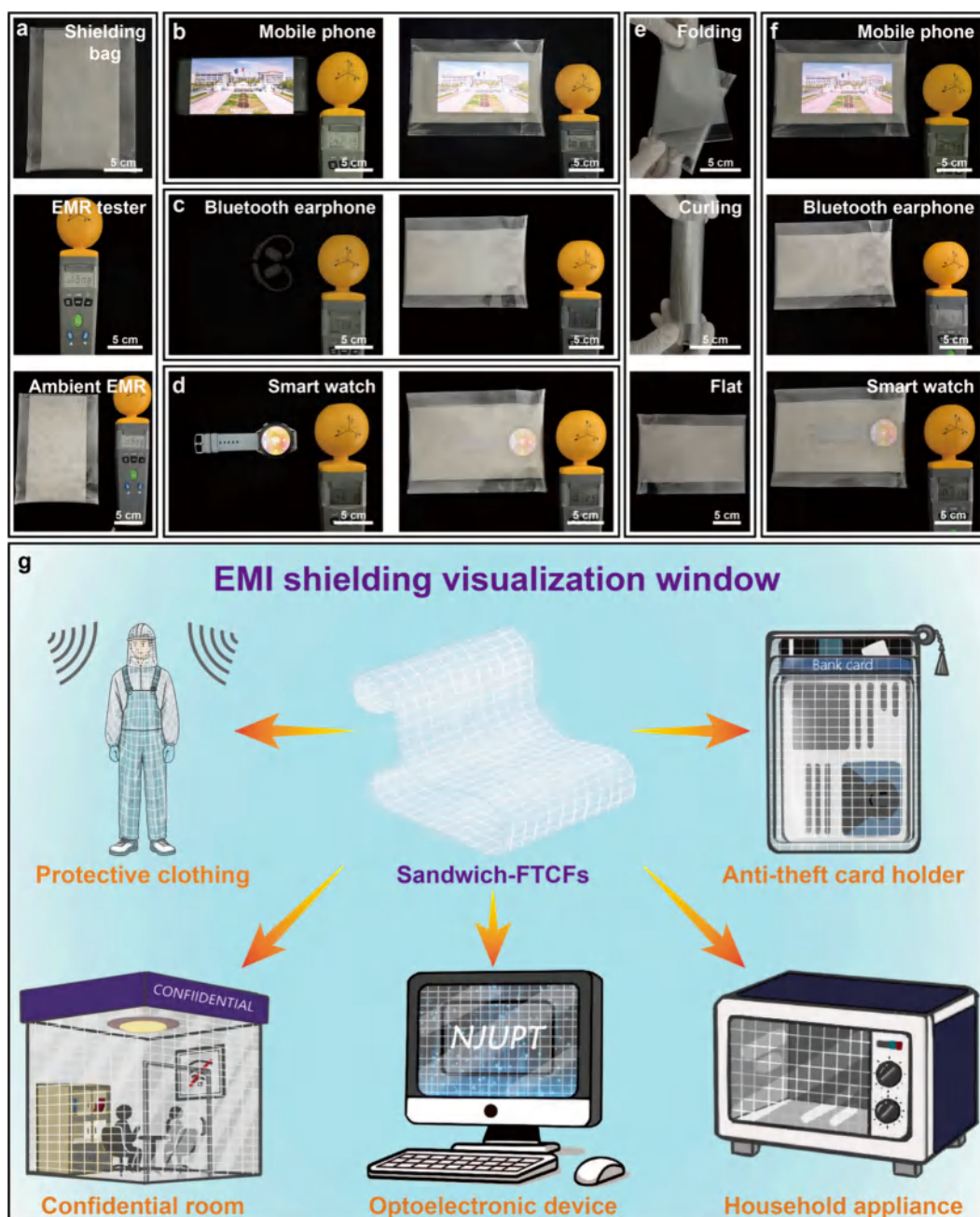


**Figure 5.** (a) Digital images of EMI shielding bag and EMR tester in an ambient environment. EMI shielding application for (b) mobile phone, (c) Bluetooth earphone, and (d) smartwatch. (e) Digital images of shielding bag being folded, curled, and returned to a flat state. (f) EMI shielding performance for the shielding bag that has returned to a flat state. (g) Demonstration diagram showcasing the other application scenarios of sandwich-FTCFs.

and  $250 \text{ mW cm}^{-2}$ , respectively. Therefore, the maximum saturation temperature of sandwich-FTCFs gradually increases with laser power density (Figure S19). Similarly, at a constant laser power density, the maximum saturation temperature increases with increasing wavelength (Figure S20). To assess the cyclic stability, we performed alternating temperature rise and cooling tests (laser on and off) at a laser power density of  $250 \text{ mW cm}^{-2}$ . Five cycles are completed within a total duration of 150 s, and the cycle curves remain consistent each time without any significant degradation in photothermal conversion performance, which indicates excellent cyclic stability of sandwich-FTCFs for photothermal response (Figure 4j). Further tests are carried out with varying laser

power densities at wavelengths of 690, 730, and 785 nm, yielding a consistent conclusion of rapid response speed and excellent cyclic stability (Figures S19 and S20). Furthermore, the EMI SE of the sandwich-FTCFs remains essentially unchanged after various environmental tests. This observation is corroborated by the corresponding changes in resistance (Figure 4), thereby further demonstrating the excellent flexibility and environmental stability of the sandwich-FTCFs (Figure S21).

**3.5. EMI Shielding Application of Sandwich-FTCFs.** Based on its exceptional EMI shielding performance, a practical application demonstration of sandwich-FTCFs is conducted to block EMR from common electronic devices.

The large-area sandwich-FTCFs ( $19 \times 10 \text{ cm}^2$ ) are first prepared. Two of these large-area sandwich-FTCFs are then combined to create an EMI shielding bag (Figure 5a). Notably, we can still expand the area of sandwich-FTCFs up to  $50 \times 50 \text{ cm}^2$  (Figure S22). The ambient EMR is measured as  $0.008 \mu\text{W cm}^{-2}$  using an EMR tester. When the shielding bag is placed near the EMR tester, there is no effect on the ambient EMR reading. The EMI SE of the shielding bag is tested by using common portable electronic devices such as mobile phones, Bluetooth earphones, and smartwatches. When the mobile phone plays a video via a cellular network, the EMR value rapidly increases from  $0.008$  to  $42.19 \mu\text{W cm}^{-2}$  (Figure 5b). However, after placing the phone inside the shielding bag, the EMR value effectively decreases to  $0.177 \mu\text{W cm}^{-2}$ , while still maintaining clear visibility of the video playing on the phone. An operating Bluetooth earphone emits an EMR with a high value of  $13.84 \mu\text{W cm}^{-2}$  (Figure 5c). Upon enclosing the earphone in the shielding bag, the EMR value plummets to  $0.155 \mu\text{W cm}^{-2}$ , which demonstrates the excellent EMI shielding capabilities of the shielding bag. While playing music, the EMR value of the smartwatch promptly increased to  $4.51 \mu\text{W cm}^{-2}$  (Figure 5d). The EMR value reduces to  $0.125 \mu\text{W cm}^{-2}$  through placing the watch in the shielding bag, and the music playback interface remains clearly visible. These tests show the splendid EMI shielding performance and high optical transmittance of shielding bag.

To further assess the durability, the shielding bag is subjected to folding and curling before returning it to a flat state (Figure 5e and Movie S4). Subsequent EMI shielding tests yield consistent results, which demonstrates the excellent durability of the shielding bag (Figure 5f). Additionally, the EMR values of the shielding bag are tested in folding, curling, and flat states while containing Bluetooth earphones and a smartwatch (Figure S23). The results indicate consistent EMR values across all three states, which further confirm the stability of the shielding bag under deformation. The numbers in the EMR tester in Figure 5a–f have been recorded in Table S2. Figure 5g illustrates the additional application scenarios for sandwich-FTCFs including protective clothing, anti-theft card holders, confidential rooms, optoelectronic devices, and household appliances.<sup>72–74</sup> These diverse applications prove the significant potential of sandwich-FTCFs in the field of EMI shielding visualization windows.

#### 4. CONCLUSION

In summary, we innovatively propose a symmetric structural optimization strategy to fabricate sandwich-FTCFs with arbitrary customized sizes and tunable EMI SE using high-precision extrusion printing technology. The sandwich-FTCFs exhibit higher EMI SE than single-layer-FTCFs with the same parameters due to the synergistic effect of multiple internal reflections and multiple-wave interference between two symmetric silver meshes. Specifically, by optimizing both line spacing and interlayer spacing, the EMI SE of sandwich-FTCFs can be improved to  $41.7 \text{ dB}$ , representing a 40% enhancement compared to that of single-layer-FTCFs. The optical transmittance of sandwich-FTCFs remains unchanged compared to single-layer-FTCFs with identical parameters due to the perfect symmetry of the dual silver mesh layers on both sides of the PET substrate. Sandwich-FTCFs also exhibit remarkable mechanical flexibility, durability, and environmental adaptability with a negligible resistance increase under diverse tests ( $0\text{--}360^\circ$  torsion test, 10,000 bending

cycles, 72 h chemical exposure, 100 min ultrasonic test, and 100 adhesion cycles). Moreover, sandwich-FTCFs demonstrate a rapid response time ( $\sim 15 \text{ s}$ ) and excellent cyclic stability in the photothermal conversion test. The successful demonstration of sandwich-FTCFs to block electromagnetic waves from a mobile phone, Bluetooth earphone, and smartwatch proves their excellent shielding performance. Consequently, the novel symmetric structural optimization strategy proposed in this work provides a viable route to fabricate FTCFs with low cost, high transmittance, and strong EMI shielding performance.

#### ■ ASSOCIATED CONTENT

##### SI Supporting Information

The Supporting Information is available free of charge at <https://pubs.acs.org/doi/10.1021/acsami.4c16375>.

Figure S1: various patterns printed on PET; Figure S2: the dimension of silver mesh at a line spacing of  $400 \mu\text{m}$ ; Figure S3: the rheological properties of the silver ink; Figure S4: photos of the silver mesh printed on different substrates; Figure S5: microscopic topography of the silver line with different line widths distributed at a spacing of  $100 \mu\text{m}$  on a PET substrate; Figure S6: cross-section SEM image of the sandwich-FTCFs; Figure S7: macroscopic and microscopic topography of sandwich-FTCFs and single-layer-FTCFs with different line spacings; Figure S8: optical transmittance of sandwich-FTCFs with line widths of  $100$  and  $150 \mu\text{m}$  at a line spacing of  $600 \mu\text{m}$ ; Figures S9–S11: EMI shielding performance, optical transmittance, macroscopic and microscopic topography of asymmetric sandwich-FTCFs with different line spacings; Figures S12, S13: EMI shielding performance and optical transmittance of single-layer-FTCFs with different PET substrate thicknesses; Figure S14: changes of the brightness for lighting an LED lamp in torsion at angles of  $90^\circ$  and  $180^\circ$ ; Figures S15–S18: macroscopic and microscopic topography of sandwich-FTCFs in chemical environmental stability tests; Figures S19, S20: temperature–time curves of sandwich-FTCFs under different conditions; Figure S21: the changes in shielding effectiveness of the sandwich-FTCFs after exposure to each environment; Figure S22: the dimension of printing platform; Figure S23: EMI shielding performance of the shielding bag in folding, curling, and flat states; Table S1: comparison in EMI SE and optical transmittance between the silver mesh-based FTCFs and other FTCFs; Table S2: the EMR value in Figure 5a–f (PDF)

Movie S1: Printing silver mesh (MP4)

Movie S2: Torsion test (MP4)

Movie S3: Bending fatigue test (MP4)

Movie S4: Flexible demonstration of shielding bag (MP4)

#### ■ AUTHOR INFORMATION

##### Corresponding Authors

Weiwei Zhao – State Key Laboratory of Organic Electronics and Information Displays and Jiangsu Key Laboratory for Biosensors, Institute of Advanced Materials (IAM), Nanjing University of Posts and Telecommunications, Nanjing 210023, People's Republic of China; [orcid.org/0000-0003-2926-8476](https://orcid.org/0000-0003-2926-8476); Email: iamwwzhao@njupt.edu.cn

**Qiang Zhao** — State Key Laboratory of Organic Electronics and Information Displays and Jiangsu Key Laboratory for Biosensors, Institute of Advanced Materials (IAM), Nanjing University of Posts and Telecommunications, Nanjing 210023, People's Republic of China; College of Electronic and Optical Engineering and College of Flexible Electronics (Future Technology), Nanjing University of Posts and Telecommunications, Nanjing 210023, People's Republic of China; [orcid.org/0000-0002-3788-4757](https://orcid.org/0000-0002-3788-4757); Email: iamqzhao@njupt.edu.cn

## Authors

**Qixiang Wang** — State Key Laboratory of Organic Electronics and Information Displays and Jiangsu Key Laboratory for Biosensors, Institute of Advanced Materials (IAM), Nanjing University of Posts and Telecommunications, Nanjing 210023, People's Republic of China

**Yuhui Feng** — State Key Laboratory of Organic Electronics and Information Displays and Jiangsu Key Laboratory for Biosensors, Institute of Advanced Materials (IAM), Nanjing University of Posts and Telecommunications, Nanjing 210023, People's Republic of China

**Feifei Lin** — State Key Laboratory of Organic Electronics and Information Displays and Jiangsu Key Laboratory for Biosensors, Institute of Advanced Materials (IAM), Nanjing University of Posts and Telecommunications, Nanjing 210023, People's Republic of China

**Yuzhe Chen** — State Key Laboratory of Organic Electronics and Information Displays and Jiangsu Key Laboratory for Biosensors, Institute of Advanced Materials (IAM), Nanjing University of Posts and Telecommunications, Nanjing 210023, People's Republic of China

**Ning Ding** — State Key Laboratory of Organic Electronics and Information Displays and Jiangsu Key Laboratory for Biosensors, Institute of Advanced Materials (IAM), Nanjing University of Posts and Telecommunications, Nanjing 210023, People's Republic of China

**Yijie Zhang** — State Key Laboratory of Organic Electronics and Information Displays and Jiangsu Key Laboratory for Biosensors, Institute of Advanced Materials (IAM), Nanjing University of Posts and Telecommunications, Nanjing 210023, People's Republic of China

**Shujuan Liu** — State Key Laboratory of Organic Electronics and Information Displays and Jiangsu Key Laboratory for Biosensors, Institute of Advanced Materials (IAM), Nanjing University of Posts and Telecommunications, Nanjing 210023, People's Republic of China

Complete contact information is available at:

<https://pubs.acs.org/10.1021/acsami.4c16375>

## Author Contributions

<sup>§</sup>Q.W. and Y.F. contributed equally to this work. Q.W., S.L., W.Z., and Q.Z. conceived and designed the study. Q.W., Y.F., F.L., Y.C., N.D., and Y.Z. performed the experiments and analyzed the data. Q.W. and Y.F. wrote the manuscript. W.Z. and Q.Z. supervised the project and provided funding support.

## Notes

The authors declare no competing financial interest.

## ACKNOWLEDGMENTS

The authors acknowledge financial support received from National Natural Science Foundation of China (62174086,

62474096, and 62288102), Outstanding Youth Foundation of Jiangsu Province (BK20240139), Innovation Support Programme (Soft Science Research) Project Achievements of Jiangsu Province (BK20231514), and Qinglan Project of Jiangsu Province of China.

## REFERENCES

- (1) Lv, H.; Yao, Y.; Li, S.; Wu, G.; Zhao, B.; Zhou, X.; Dupont, R. L.; Kara, U. I.; Zhou, Y.; Xi, S.; Liu, B.; Che, R.; Zhang, J.; Xu, H.; Adera, S.; Wu, R.; Wang, X. Staggered Circular Nanoporous Graphene Converts Electromagnetic Waves into Electricity. *Nat. Commun.* **2023**, *14*, 1982.
- (2) Zhang, Y.; Ruan, K.; Zhou, K.; Gu, J. Controlled Distributed  $Ti_3C_2T_x$  Hollow Microspheres on Thermally Conductive Polyimide Composite Films for Excellent Electromagnetic Interference Shielding. *Adv. Mater.* **2023**, *35*, 2211642.
- (3) Li, P.; Wang, H.; Ju, Z.; Jin, Z.; Ma, J.; Yang, L.; Zhao, X.; Xu, H.; Liu, Y.  $Ti_3C_2T_x$  MXene-and Sulfuric Acid-Treated Double-Network Hydrogel with Ultralow Conductive Filler Content for Stretchable Electromagnetic Interference Shielding. *ACS Nano* **2024**, *18*, 2906–2916.
- (4) Zhang, X.; Tian, X.; Wu, N.; Zhao, S.; Qin, Y.; Pan, F.; Yue, S.; Ma, X.; Qiao, J.; Xu, W.; Liu, W.; Liu, J.; Zhao, M.; Ostrikov, K.; Zeng, Z. Metal-Organic Frameworks with Fine-Tuned Interlayer Spacing for Microwave Absorption. *Sci. Adv.* **2024**, *10*, No. eadl6498.
- (5) Ma, D.; Ji, M.; Yi, H.; Wang, Q.; Fan, F.; Feng, B.; Zheng, M.; Chen, Y.; Duan, H. Pushing the Thinness Limit of Silver Films for Flexible Optoelectronic Devices via Ion-Beam Thinning-Back Process. *Nat. Commun.* **2024**, *15*, 2248.
- (6) Luo, S.; Lian, E.; He, J.; deMello, J. C. Flexible Transparent Electrodes Formed from Template-Patterned Thin-Film Silver. *Adv. Mater.* **2024**, *36*, 2300058.
- (7) Qiu, T.; Akinoglu, E. M.; Luo, B.; Konarova, M.; Yun, J. H.; Gentle, I. R.; Wang, L. Nanosphere Lithography: A Versatile Approach to Develop Transparent Conductive Films for Optoelectronic Applications. *Adv. Mater.* **2022**, *34*, 2103842.
- (8) Jin, M.; Chen, W.; Liu, L. X.; Zhang, H. B.; Ye, L.; Min, P.; Yu, Z. Z. Transparent, Conductive and Flexible MXene Grid/Silver Nanowire Hierarchical Films for High-Performance Electromagnetic Interference Shielding. *J. Mater. Chem. A* **2022**, *10*, 14364–14373.
- (9) Li, M.; Zarei, M.; Mohammadi, K.; Walker, S. B.; LeMieux, M.; Leu, P. W. Silver Meshes for Record-Performance Transparent Electromagnetic Interference Shielding. *ACS Appl. Mater. Interfaces* **2023**, *15*, 30591–30599.
- (10) Feng, Y.; Song, J.; Han, G.; Zhou, B.; Liu, C.; Shen, C. Transparent and Stretchable Electromagnetic Interference Shielding Film with Fence-Like Aligned Silver Nanowire Conductive Network. *Small Methods* **2023**, *7*, 2201490.
- (11) Yang, Y.; Chen, S.; Li, W.; Li, P.; Ma, J.; Li, B.; Zhao, X.; Ju, Z.; Chang, H.; Xiao, L.; Xu, H.; Liu, Y. Reduced Graphene Oxide Conformally Wrapped Silver Nanowire Networks for Flexible Transparent Heating and Electromagnetic Interference Shielding. *ACS Nano* **2020**, *14*, 8754–8765.
- (12) Yuan, S.; Fan, Z.; Wang, G.; Chai, Z.; Wang, T.; Zhao, D.; Busnaina, A. A.; Lu, X. Fabrication of Flexible and Transparent Metal Mesh Electrodes Using Surface Energy-Directed Assembly Process for Touch Screen Panels and Heaters. *Adv. Sci.* **2023**, *10*, 2304990.
- (13) Li, Z.; Li, H.; Zhu, X.; Peng, Z.; Zhang, G.; Yang, J.; Wang, F.; Zhang, Y.-F.; Sun, L.; Wang, R.; Zhang, J.; Yang, Z.; Yi, H.; Lan, H. Directly Printed Embedded Metal Mesh for Flexible Transparent Electrode via Liquid Substrate Electric-Field-Driven Jet. *Adv. Sci.* **2022**, *9*, 2105331.
- (14) Cheng, M.; Ying, M.; Zhao, R.; Ji, L.; Li, H.; Liu, X.; Zhang, J.; Li, Y.; Dong, X.; Zhang, X. Transparent and Flexible Electromagnetic Interference Shielding Materials by Constructing Sandwich AgNW@MXene/Wood Composites. *ACS Nano* **2022**, *16*, 16996–17007.

- (15) Isari, A. A.; Ghaffarkhah, A.; Hashemi, S. A.; Wuttke, S.; Arjmand, M. Structural Design for EMI Shielding: From Underlying Mechanisms to Common Pitfalls. *Adv. Mater.* **2024**, *36*, 2310683.
- (16) Hu, G.; Wu, C.; Wang, Q.; Dong, F.; Xiong, Y. Ultrathin Nanocomposite Films with Asymmetric Gradient Alternating Multi-layer Structures Exhibit Superhigh Electromagnetic Interference Shielding Performances and Robust Mechanical Properties. *Chem. Eng. J.* **2022**, *447*, 137537.
- (17) Li, L.; Yan, Y.; Liang, J.; Zhao, J.; Lyu, C.; Zhai, H.; Wu, X.; Wang, G. Wearable EMI Shielding Composite Films with Integrated Optimization of Electrical Safety, Biosafety and Thermal Safety. *Adv. Sci.* **2024**, *11*, 2400887.
- (18) Chen, W.; Liu, L. X.; Zhang, H. B.; Yu, Z. Z. Flexible, Transparent, and Conductive  $Ti_3C_2T_x$  MXene-Silver Nanowire Films with Smart Acoustic Sensitivity for High-Performance Electromagnetic Interference Shielding. *ACS Nano* **2020**, *14*, 16643–16653.
- (19) Zhao, W.; Xu, H.; Zhao, J.; Zhu, X.; Lu, Y.; Ding, C.; He, W.; Bian, J.; Liu, L.; Ma, L.; Wang, W.; Zhou, T.; Zhou, X.; Li, J.; Liu, S.; Zhao, Q. Flexible, Lightweight and Multi-Level Superimposed Titanium Carbide Films for Enhanced Electromagnetic Interference Shielding. *Chem. Eng. J.* **2022**, *437*, 135266.
- (20) Saadi, M.; Maguire, A.; Pottackal, N. T.; Thakur, M. S. H.; Ikram, M. M.; Hart, A. J.; Ajayan, P. M.; Rahman, M. M. Direct Ink Writing: A 3D Printing Technology for Diverse Materials. *Adv. Mater.* **2022**, *34*, 2108855.
- (21) Yan, J.; Huang, S.; Lim, Y. V.; Xu, T.; Kong, D.; Li, X.; Yang, H. Y.; Wang, Y. Direct-Ink Writing 3D Printed Energy Storage Devices: From Material Selectivity, Design and Optimization Strategies to Diverse Applications. *Mater. Today* **2022**, *54*, 110–152.
- (22) Chen, L.; Mai, T.; Ji, X. X.; Wang, P. L.; Qi, M. Y.; Liu, Q.; Ding, Y.; Ma, M. G. 3D Printing of Customizable and Lightweight Multilayer MXene/Nanocellulose Architectures for Tunable Electromagnetic Interference Shielding via Direct Ink Writing. *Chem. Eng. J.* **2023**, *476*, 146652.
- (23) Qi, C. Z.; Wu, X.; Liu, J.; Luo, X. J.; Zhang, H. B.; Yu, Z. Z. Highly Conductive Calcium Ion-Reinforced MXene/Sodium Alginate Aerogel Meshes by Direct Ink Writing for Electromagnetic Interference Shielding and Joule Heating. *J. Mater. Sci. Technol.* **2023**, *135*, 213–220.
- (24) Park, S. Y.; Lee, S.; Yang, J.; Kang, M. S. Patterning Quantum Dots via Photolithography: A Review. *Adv. Mater.* **2023**, *35*, 2300546.
- (25) Bathaei, M. J.; Singh, R.; Mirzajani, H.; Istif, E.; Akhtar, M. J.; Abbasiasl, T.; Beker, L. Photolithography-Based Microfabrication of Biodegradable Flexible and Stretchable Sensors. *Adv. Mater.* **2023**, *35*, 2207081.
- (26) Zhang, Y.; Lu, Z.; Zhou, X.; Xiong, J. Metallic Meshes for Advanced Flexible Optoelectronic Devices. *Mater. Today* **2024**, *73*, 179–207.
- (27) Wu, X.; Tu, T.; Dai, Y.; Tang, P.; Zhang, Y.; Deng, Z.; Li, L.; Zhang, H. B.; Yu, Z. Z. Direct Ink Writing of Highly Conductive MXene Frames for Tunable Electromagnetic Interference Shielding and Electromagnetic Wave-Induced Thermochromism. *Nano-Micro Lett.* **2021**, *13*, 148.
- (28) Tyagi, B.; Lee, H. B.; Kumar, N.; Jin, W. Y.; Ko, K. J.; Ovhal, M. M.; Sahani, R.; Chung, H. J.; Seo, J.; Kang, J. W. High-Performance, Large-Area Semitransparent and Tandem Perovskite Solar Cells Featuring Highly Scalable a-ITO/Ag Mesh 3D Top Electrodes. *Nano Energy* **2022**, *95*, 106978.
- (29) Nan, Z.; Wei, W.; Lin, Z.; Chang, J.; Hao, Y. Flexible Nanocomposite Conductors for Electromagnetic Interference Shielding. *Nano-Micro Lett.* **2023**, *15*, 172.
- (30) Liang, C.; Gu, Z.; Zhang, Y.; Ma, Z.; Qiu, H.; Gu, J. Structural Design Strategies of Polymer Matrix Composites for Electromagnetic Interference Shielding: A Review. *Nano-Micro Lett.* **2021**, *13*, 181.
- (31) Liu, J.; Yu, M. Y.; Yu, Z. Z.; Nicolosi, V. Design and Advanced Manufacturing of Electromagnetic Interference Shielding Materials. *Mater. Today* **2023**, *66*, 245–272.
- (32) Zhang, Y.; Ruan, K.; Gu, J. Flexible Sandwich-Structured Electromagnetic Interference Shielding Nanocomposite Films with Excellent Thermal Conductivities. *Small* **2021**, *17*, 2101951.
- (33) Yuan, C.; Huang, J.; Dong, Y.; Huang, X.; Lu, Y.; Li, J.; Tian, T.; Liu, W.; Song, W. Record-High Transparent Electromagnetic Interference Shielding Achieved by Simultaneous Microwave Fabry-Pérot Interference and Optical Antireflection. *ACS Appl. Mater. Interfaces* **2020**, *12*, 26659–26669.
- (34) Du, Z.; Zhang, G.; Chen, K.; Zhou, C.; Zhu, X.; Zhang, Y.; Chen, K.; Mi, H.-Y.; Wang, Y.; Liu, C.; Shen, C. MXene/Polylactic Acid Fabric-Based Resonant Cavity for Realizing Simultaneous High-Performance Electromagnetic Interference (EMI) Shielding and Efficient Energy Harvesting. *ACS Appl. Mater. Interfaces* **2022**, *14*, 14607–14617.
- (35) Chen, Z.; Yang, S.; Huang, J.; Gu, Y.; Huang, W.; Liu, S.; Lin, Z.; Zeng, Z.; Hu, Y.; Chen, Z.; Yang, B.; Gui, X. Flexible, Transparent and Conductive Metal Mesh Films with Ultra-High FoM for Stretchable Heating and Electromagnetic Interference Shielding. *Nano-Micro Lett.* **2024**, *16*, 92.
- (36) Yang, J.; Zhou, B.; Han, D.; Cui, N.; Li, B.; Shen, J.; Zhang, Z.; Du, A. High-Precision Three-Dimensional Printing in a Flexible, Low-Cost and Versatile Way: A Review. *ES Mater. Manuf.* **2021**, *15*, 1–13.
- (37) Kuang, M.; Wang, L.; Song, Y. Controllable Printing Droplets for High-Resolution Patterns. *Adv. Mater.* **2014**, *26*, 6950–6958.
- (38) Fukuda, K.; Someya, T. Recent Progress in the Development of Printed Thin-Film Transistors and Circuits with High-Resolution Printing Technology. *Adv. Mater.* **2017**, *29*, 1602736.
- (39) Saadi, M. A. S. R.; Maguire, A.; Pottackal, N. T.; Thakur, M. S. H.; Ikram, M. M.; Hart, A. J.; Ajayan, P. M.; Rahman, M. M. Direct Ink Writing: A 3D Printing Technology for Diverse Materials. *Adv. Mater.* **2022**, *34*, 2108855.
- (40) Estelle, K. T.; Gozen, B. A. Complex Ink Flow Mechanisms in Micro-Direct-Ink-Writing and Their Implications on Flow Rate Control. *Addit. Manuf.* **2022**, *59*, 103183.
- (41) Xu, Z.; Wang, X.; Chen, F.; Chen, K. Effect of Fumed Silica Nanoparticles on the Performance of Magnetically Active Inks and DIW Printing. *ACS Appl. Polym. Mater.* **2023**, *5*, 5794–5804.
- (42) Baniasadi, H.; Abidnejad, R.; Fazeli, M.; Lipponen, J.; Niskanen, J.; Kontturi, E.; Seppälä, J.; Rojas, O. J. Innovations in Hydrogel-Based Manufacturing: A Comprehensive Review of Direct Ink Writing Technique for Biomedical Applications. *Adv. Colloid Interface Sci.* **2024**, *324*, 103095.
- (43) Zheng, Q.; Xie, B.; Xu, Z.; Wu, H. A Systematic Printability Study of Direct Ink Writing Towards High-Resolution Rapid Manufacturing. *Int. J. Extreme Manuf.* **2023**, *5*, 035002.
- (44) Li, H.; Zhang, Y.; Tai, Y.; Zhu, X.; Qi, X.; Zhou, L.; Li, Z.; Lan, H. Flexible Transparent Electromagnetic Interference Shielding Films with Silver Mesh Fabricated Using Electric-Field-Driven Microscale 3D Printing. *Opt. Laser Technol.* **2022**, *148*, 107717.
- (45) Kong, X.; Li, H.; Wang, J.; Wang, Y.; Zhang, L.; Gong, M.; Lin, X.; Wang, D. Direct Writing of Silver Nanowire Patterns with Line Width Down to 50  $\mu$ m and Ultrahigh Conductivity. *ACS Appl. Mater. Interfaces* **2023**, *15*, 9906–9915.
- (46) Kelly, A. G.; Sheil, S.; Douglas-Henry, D. A.; Caffrey, E.; Gabbett, C.; Doolan, L.; Nicolosi, V.; Coleman, J. N. Transparent Conductors Printed from Grids of Highly Conductive Silver Nanosheets. *ACS Appl. Mater. Interfaces* **2023**, *15*, 39864–39871.
- (47) Kelly, A. G.; O'Reilly, J.; Gabbett, C.; Szydłowska, B.; O'Suilleabhain, D.; Khan, U.; Maughan, J.; Carey, T.; Sheil, S.; Stamenov, P.; Coleman, J. N. Highly Conductive Networks of Silver Nanosheets. *Small* **2022**, *18*, 2105996.
- (48) Shahzad, F.; Alhabeb, M.; Hatter, C. B.; Anasori, B.; Man Hong, S.; Koo, C. M.; Gogotsi, Y. Electromagnetic Interference Shielding with 2D Transition Metal Carbides (MXenes). *Science* **2016**, *353*, 1137–1140.
- (49) Peng, M.; Qin, F. Clarification of Basic Concepts for Electromagnetic Interference Shielding Effectiveness. *J. Appl. Phys.* **2021**, *130*, 225108.

- (50) Jia, X.; Li, Y.; Shen, B.; Zheng, W. Evaluation, Fabrication and Dynamic Performance Regulation of Green EMI-Shielding Materials with Low Reflectivity: A Review. *Composites, Part B* **2022**, *233*, 109652.
- (51) Verma, R.; Thakur, P.; Chauhan, A.; Jasrotia, R.; Thakur, A. A Review on MXene and Its' Composites for Electromagnetic Interference (EMI) Shielding Applications. *Carbon* **2023**, *208*, 170–190.
- (52) Wang, G.; Zhao, Y.; Yang, F.; Zhang, Y.; Zhou, M.; Ji, G. Multifunctional Integrated Transparent Film for Efficient Electromagnetic Protection. *Nano-Micro Lett.* **2022**, *14*, 65.
- (53) Peng, F.; Zhu, W.; Fang, Y.; Fu, B.; Chen, H.; Ji, H.; Ma, X.; Hang, C.; Li, M. Ultralight and Highly Conductive Silver Nanowire Aerogels for High-Performance Electromagnetic Interference Shielding. *ACS Appl. Mater. Interfaces* **2023**, *15*, 4284–4293.
- (54) Iqbal, A.; Sambyal, P.; Koo, C. M. 2D MXenes for Electromagnetic Shielding: A Review. *Adv. Funct. Mater.* **2020**, *30*, 2000883.
- (55) Yang, S.; Lin, Z.; Wang, X.; Huang, J.; Yang, R.; Chen, Z.; Jia, Y.; Zeng, Z.; Cao, Z.; Zhu, H.; Hu, Y.; Li, E.; Chen, H.; Wang, T.; Deng, S.; Gui, X. Stretchable, Transparent, and Ultra-Broadband Terahertz Shielding Thin Films Based on Wrinkled MXene Architectures. *Nano-Micro Lett.* **2024**, *16*, 165.
- (56) Ma, C.; Cao, W. T.; Zhang, W.; Ma, M. G.; Sun, W. M.; Zhang, J.; Chen, F. Wearable, Ultrathin and Transparent Bacterial Celluloses/MXene Film with Janus Structure and Excellent Mechanical Property for Electromagnetic Interference Shielding. *Chem. Eng. J.* **2021**, *403*, 126438.
- (57) Li, Q.; Sun, Y.; Zhou, B.; Han, G.; Feng, Y.; Liu, C.; Shen, C. Flexible, Stretchable, and Transparent MXene Nanosheet/Thermoplastic Polyurethane Films for Multifunctional Heating and Electromagnetic Interference Shielding. *ACS Appl. Nano Mater.* **2023**, *6*, 3395–3404.
- (58) Chizari, K.; Arjmand, M.; Liu, Z.; Sundararaj, U.; Therriault, D. Three-Dimensional Printing of Highly Conductive Polymer Nanocomposites for EMI Shielding Applications. *Mater. Today Commun.* **2017**, *11*, 112–118.
- (59) Hong, W.; Sun, B.; Li, Z.; Fu, Z.; Zhang, J.; Jiang, M.; Zhang, Y.; Li, Y.; Zhang, Y.; Qian, K. Biodegradable, Flexible Transparent Ordered Ag NWs Micromesh Conductor for Electrical Heater and Electromagnetic Interference Shielding Applications. *ACS Appl. Electron. Mater.* **2022**, *4*, 5446–5455.
- (60) Zhou, B.; Su, M.; Yang, D.; Han, G.; Feng, Y.; Wang, B.; Ma, J.; Ma, J.; Liu, C.; Shen, C. Flexible MXene/Silver Nanowire-Based Transparent Conductive Film with Electromagnetic Interference Shielding and Electro-Photo-Thermal Performance. *ACS Appl. Mater. Interfaces* **2020**, *12*, 40859–40869.
- (61) Li, Z.; Che, W.; Jiang, Y.; Liu, Y.; Fang, X.; Peng, Y. Strong, Hydrophobic, and Transparent Wood Film Decorated with MXene/Silver Nanowire for Electromagnetic Interference Shielding and Electrothermal Conversion. *Colloids Surf., A* **2023**, *676*, 132211.
- (62) Weng, G.-M.; Li, J.; Alhabeb, M.; Karpovich, C.; Wang, H.; Lipton, J.; Maleski, K.; Kong, J.; Shaulsky, E.; Elimelech, M.; Gogotsi, Y.; Taylor, A. D. Layer-by-Layer Assembly of Cross-Functional Semi-Transparent MXene-Carbon Nanotubes Composite Films for Next-Generation Electromagnetic Interference Shielding. *Adv. Funct. Mater.* **2018**, *28*, 1803360.
- (63) Li, Z.; Li, Y.; Zhao, W.; Feng, Y.; Zhou, B.; Liu, C. Flexible, Hierarchical MXene@ SWNTs Transparent Conductive Film with Multi-Source Thermal Response for Electromagnetic Interference Shielding. *Compos. Sci. Technol.* **2024**, *249*, 110484.
- (64) Zhang, N.; Wang, Z.; Song, R.; Wang, Q.; Chen, H.; Zhang, B.; Lv, H.; Wu, Z.; He, D. Flexible and Transparent Graphene/Silver-Nanowires Composite Film for High Electromagnetic Interference Shielding Effectiveness. *Sci. Bull.* **2019**, *64*, 540–546.
- (65) Zhou, B.; Li, Z.; Li, Y.; Liu, X.; Ma, J.; Feng, Y.; Zhang, D.; He, C.; Liu, C.; Shen, C. Flexible Hydrophobic 2D  $Ti_3C_2T_x$ -Based Transparent Conductive Film with Multifunctional Self-Cleaning, Electromagnetic Interference Shielding and Joule Heating Capacities. *Compos. Sci. Technol.* **2021**, *201*, 108531.
- (66) Park, S. I.; Ahn, J. H.; Feng, X.; Wang, S.; Huang, Y.; Rogers, J. A. Theoretical and Experimental Studies of Bending of Inorganic Electronic Materials on Plastic Substrates. *Adv. Funct. Mater.* **2008**, *18*, 2673–2684.
- (67) Kim, D.; Kim, S. H.; Kim, J. H.; Lee, J. C.; Ahn, J. P.; Kim, S. W. Failure Criterion of Silver Nanowire Electrodes on a Polymer Substrate for Highly Flexible Devices. *Sci. Rep.* **2017**, *7*, 45903.
- (68) Zhu, X.; Liu, M.; Qi, X.; Li, H.; Zhang, Y.-F.; Li, Z.; Peng, Z.; Yang, J.; Qian, L.; Xu, Q.; Gou, N.; He, J.; Li, D.; Lan, H. Templateless, Plating-Free Fabrication of Flexible Transparent Electrodes with Embedded Silver Mesh by Electric-Field-Driven Microscale 3D Printing and Hybrid Hot Embossing. *Adv. Mater.* **2021**, *33*, 2007772.
- (69) Li, L.; Zhu, Y. J. High Chemical Reactivity of Silver Nanoparticles toward Hydrochloric Acid. *J. Colloid Interface Sci.* **2006**, *303*, 415–418.
- (70) Li, Q.; Huang, F.; Li, S.; Zhang, H.; Yu, X. Y. Oxygen Vacancy Engineering Synergistic with Surface Hydrophilicity Modification of Hollow Ru Doped CoNi-LDH Nanotube Arrays for Boosting Hydrogen Evolution. *Small* **2022**, *18*, 2104323.
- (71) Huang, Y.; Yu, Q.; Li, M.; Jin, S.; Fan, J.; Zhao, L.; Yao, Z. Surface Modification of Activated Carbon Fiber by Low-Temperature Oxygen Plasma: Textural Property, Surface Chemistry, and the Effect of Water Vapor Adsorption. *Chem. Eng. J.* **2021**, *418*, 129474.
- (72) Fan, Z.; Lu, L.; Sang, M.; Wu, J.; Wang, X.; Xu, F.; Gong, X.; Luo, T.; Leung, K. C. F.; Xuan, S. Wearable Safeguarding Leather Composite with Excellent Sensing, Thermal Management, and Electromagnetic Interference Shielding. *Adv. Sci.* **2023**, *10*, 2302412.
- (73) Wang, X.; Lei, Z.; Ma, X.; He, G.; Xu, T.; Tan, J.; Wang, L.; Zhang, X.; Qu, L.; Zhang, X. A Lightweight MXene-Coated Nonwoven Fabric with Excellent Flame Retardancy, EMI Shielding, and Electrothermal/Photothermal Conversion for Wearable Heater. *Chem. Eng. J.* **2022**, *430*, 132605.
- (74) Wang, X.; Shi, T.; Wan, C.; Zong, P. A.; Liu, Z.; Huang, W. Co-Enhanced Electromagnetic Shielding and Thermoelectric Performance in  $Bi_2Te_3$  Coated Carbon Cloth. *Carbon* **2023**, *213*, 118298.